Check for updates

▍ Inorganic Chemistry

Molecular Imaging Contrast Properties of Fe$_3$O$_4$-Au Hybrid Nanoparticles for Dual-Mode MR/CT Imaging Applications

Hoa Du Nguyen,[a] The Tam Le,*[a] Thi Ngoc Linh Nguyen,*[b] Thi Hong Tuyet Phan,[a] Dinh Quang Ho,[a] Hong Nam Pham,[c, e] Thien Vuong Nguyen,[d, e] Trong Lu Le,[d, e] and Lam Dai Tran[d, e]

The development of noninvasive testing techniques in medicine by combining dual-mode Magnetic Resonance (MR)/ Computed Tomography (CT) imaging techniques will help overcome the limitations of the separated methods, leading to more accurate diagnoses. This has implications in clinical research, but currently remains a major challenge in terms of the need for a corresponding multimodal signal contrast agent. In this study, we use small size, monodispersed Fe$_3$O$_4$ magnetic nanoparticles as the seeds to synthesize magneto-plasmonic Fe$_3$O$_4$@Au hybrid nanoparticles (HNPs) with multiple functions with core-shell structures. The influence of the ratios of HAuCl$_4$ and oleyamine (OLA) precursors on the shape and size of the nanoparticles (NPs) was investigated. The HAuCl$_4$/OLA ratio of 0.2/1 is the optimal condition. The obtained NPs has an average size of 21.2 nm with a uniform spherical shape, high monodispersity. After the surface functionalization with poly(acrylic acid) (PAA), the resulting Fe$_3$O$_4$@Au@PAA HNPs showed excellent dispersion in water, good biocompatibility, non-

toxicity against Hep-G2 cancer cell line and Vero healthy cell line at high test concentration. The *In-vitro* test data showed that the materials with Au shell enhance X-ray decrease even at low concentrations compared to iodine-based commercial substances while retaining the same effect as T$_2$ contrast agent with high transverse relaxation rate r$_2$ (125.2 mM^{-1}s^{-1}). The *In-vivo* MRI images of rat liver tissue demonstrated that the hybrid nanoparticles showed the contrast increases 3 times under 1.5 T magnetic field after 30 minutes of drug administration. The computed tomography measurements showed the highest Hounsfield unit (HU) of 133.5 after the hybrid nanoparticle injected for 30 minutes. The *in-vivo* efficacy of Fe$_3$O$_4$@Au@PAA magneto-plasmonic hybrid nanoparticles was further evaluated in the cardiac and renal organs in a mouse test model to study drug kinetics. Generally, these Fe$_3$O$_4$@Au@PAA hybrid nanomaterials showed great promise as a candidate for multimodality molecular bio-imaging.

1. Introduction

The current molecular imaging techniques enhance disease diagnosis capacity by monitoring cellular functions and conversion processes at the molecular level in living organisms. However, due to the limitations of every individual technique, no single molecular imaging technique provides full information about the structure and function of living organisms. In

recent years, dual-mode molecular imaging techniques, such as MR/fluorescence, MR/PET,[1] CT/PET,[2] MR/CT,[3] PET/SPECT,[4] CT/ NIR fluorescence,[5] or MR/optical imaging[6] has been studied and used in medical practice. The outstanding advantages of MRI technique are clear, sharp, high-resolution, and multi-plane images, without using high-energy radiation or other biological effects, consequently the high safety. However, MRI requires a long measurement time of tens of minutes, and is less effective for diagnosing injuries of bone, or any ralated to calcification, such as atherosclerosis. Therefore, CT scanning which provides high spatial resolution, greater density than other images, especially very fast scan time is used. For these reasons, the combination of MR/CT imaging techniques will help overcome the limitations of separated methods, allow to diagnose diseases more accurately.[7–9]

To improve molecular imaging quality in MRI technique, several magnetic nanomaterials, such as oxides and ferrites of some 3d series transition metals (Fe, Co or Mn), have been used as T$_2$ contrast agents.[10–12] Meanwhile, the trend of replacing iodine compounds in CT techniques due to their side effects has led to research on gold nanoparticles due to their biocompatibility, safety, and greater X-ray attenuation coefficient. Therefore, the study of these nanomaterials with different compositions and properties in a hybrid materials system

[a] Prof. H. D. Nguyen, Dr. T. T. Le, Prof. T. H. T. Phan, Dr. D. Q. Ho
Vinh University, 182 Le Duan, Vinh City 460000, Vietnam
E-mail: tamlt@vinhuni.edu.vn

[b] Dr. T. N. L. Nguyen
Thai Nguyen University of Sciences, Tan Thinh Ward, Thai Nguyen City 250000, Vietnam
E-mail: linhntn@tnus.edu.vn

[c] Dr. H. N. Pham
Institute of Materials Science, Vietnam Academy of Science and Technology, 18 Hoang Quoc Viet Road, Hanoi 100000, Vietnam

[d] Dr. T. V. Nguyen, Dr. T. L. Le, Prof. L. D. Tran
Institute for Tropical Technology, Vietnam Academy of Science and Technology, 18 Hoang Quoc Viet Road, Hanoi 100000, Vietnam

[e] Dr. H. N. Pham, Dr. T. V. Nguyen, Dr. T. L. Le, Prof. L. D. Tran
Graduate University of Science and Technology, Vietnam Academy of Science and Technology, 18 Hoang Quoc Viet Road, Hanoi 100000, Vietnam

ChemistrySelect

Full Papers
doi.org/10.1002/slct.202102791

Chemistry
Europe
European Chemical
Societies Publishing

may not only integrate their characteristics but also improve them or earn new properties due to the interaction between the combinatorial components.[1–3,6,7,13–15]

E. Fantechi et al. synthesized Au-Fe$_3$O$_4$ hetero-structured nanocrystals (HNCs) by thermal decomposition of the iron precursors in the presence of preformed Au 10 nm metal nanocrystals.[16] This study showed that the nucleation of Fe$_3$O$_4$ on Au particles is more sensitive to the iron precursors and the reaction conditions than the formation of normal homogeneous Fe$_3$O$_4$ NPs. Fe(acac)$_3$ is also found to be more sensitive to the conditions than Fe(CO)$_5$. Chenjie Xu et al. have synthesized biocompatible Au-Fe$_3$O$_4$ hybrid nanoparticles with the dumbbell structure, which can be used as magnetic and optical probes for cell imaging applications.[17] Fe$_3$O$_4$/Au nanoparticles were firstly synthesized by decomposing iron pentacarbonyl on the surface of Au nanoparticles in the presence of oleic acid and oleylamine.[18] Fe$_3$O$_4$ 20 nm particles, Au-Fe$_3$O$_4$ nano dumb-bells and A431 cells are marked with 8–20 nm Au-Fe$_3$O$_4$ nanoparticles all shortened the T$_2$ transverse relaxation time of water molecules, thus increasing the image contrast in MRI technique.[17]

Yongdong Jin et al. showed that Fe$_3$O$_4$@polyme@Au hybrid particles have a magnetic core and Au shell separated by a dielectric polymer layer, light absorbability in the NIR region, allowing to enhance magnetic resonance imaging contrast (MRI) according to T2-weighted (T2 W) and photoelectromagnetic imaging.[19] Xiaoyuan Chen et al. have fabricated Fe$_3$O$_4$@Au hollow hybrid system with a porous Au shell, integrating both magnetic and optical properties (in the NIR region), which can be used as a multimodal image contrast agent, and also supply high optical-thermal conversion efficiency.[20]

By the one-step hydrothermal method, Jingchao Li et al. synthesized Fe$_3$O$_4$@Au hybrid nanomaterials, which has transverse relaxation rate high r$_2$ (146.07 mM^{-1}s^{-1}) and good X-ray attenuation properties, allowing to use them as contrast agents for MRI/CT imaging of the mouse liver and aorta.[21] However, the CT signal from the Fe$_3$O$_4$@Au composite was obtained at a high concentration of Au precursor, which resulted in a large amount of the material needed. Moreover, due to the synthesis in the aqueous environment, the resulting nanoparticles are not of high quality, large in size, easy to be clustered. The particles are not uniform in size and different in shape.

In our recent researches,[22–24] Fe$_3$O$_4$ magnetic nanoparticles were synthesized by thermal decomposition method under optimal conditions, using inorganic ferrous salt precursors and 1-octadecanol (OCD-ol) as an alternative to 1,2-hexadecandiol to reduce the fabrication costs. The obtained materials has a high transverse relaxation rate r$_2$ value, reaching 158.4 mM^{-1}s^{-1}, which is unaffected over a wide pH and high NaCl concentration. The in-vivo test results on rabbits showed clear MRI images of the livers, kidneys, and other organs in the T2-weighted imaging mode, the retention time of contrast materials in the body can be extended to 90 minutes.

In this work, we used Fe$_3$O$_4$ nanoparticles with small size, monodispersed as the seeds to synthesize magneto-plasmonic hybrid nanoparticles with a core-shell structure. The influence

of HAuCl$_4$ and oleyamine (OLA) ratios on the shape and size of the obtained NPs will be investigated to find the optimal conditions. Magneto-plasmonic hybrid nanoparticles will be surface-functionalized with polyacrylic acid (PAA) to produce highly dispersed particles in water. The core-shell structural materials with thick Au shells to reduce core magnetism will be studied to evaluate their ability as T$_2$ contrast agents and X-ray attenuation ability in CT imaging. The In-vivo experiments were conducted to evaluate the toxicity and usability as a dual contrast agent for MR/CT of the materials.

2. Results and discussion

2.1. Characterization of Fe$_3$O$_4$ NPs

The synthesis process of Fe$_3$O$_4$@Au hybrid nanoparticles is described in Figure 1. In the first stage, Fe$_3$O$_4$ nanoparticles are prepared by decomposing Fe(acac)$_3$ precursors in ODE solvent at high temperature. The second step is to prepare Fe$_3$O$_4$@Au hybrid NPs by seed-mediated growth method. Fe$_3$O$_4$ NPs were used as the seeds. HAuCl$_4$ is Au precursor and OLA acts as both reducing agent and surface-active ligand. In the solution, initially, an Au-oleylamine complex is formed. OLA then reduces Au(III) to Au metal, which crytallizes on Fe$_3$O$_4$ NPs surface forming core-shell structure Fe$_3$O$_4$@Au HNPs.

Figure 1 showed TEM images and size distribution histogram of Fe$_3$O$_4$ NPs and Fe$_3$O$_4$@Au hybrid NPs synthesized at different mole ratios of HAuCl$_4$/OLA. The results indicated that the Fe$_3$O$_4$ NPs are monodispersed with an average size of around 7.8 ± 0.7 nm (Figure 1a).[22] Meanwhile, the morphology and size of Fe$_3$O$_4$@Au hybrid NPs depend on the mole ratio of precursor and surface-active agents (HAuCl$_4$/OLA) (Figure 1b–e). This can be explained by LaMer mechanism and Ostwald effect. At the ratio HAuCl$_4$/OLA = 0.1:1 (Figure 1b), the obtained materials still contain many small particles of the original Fe$_3$O$_4$ seeds, indicating that there is no Au deposition on them when the HAuCl$_4$ concentration is low. In this case, the amount of Au atoms formed via the redox reaction is not enough for nucleation to crystallize Au on all Fe$_3$O$_4$ seeds. In the sample with the HAuCl$_4$/OLA ratio 0.2:1, the nanoparticles obtained were uniform in size of about 21.2 ± 1.3 nm and monodisperse (Figure 1d), without the initial Fe$_3$O$_4$ particles. This indicated that at a sufficiently large ratio of precursors, the amount of Au atoms was large enough to form uniform deposition on the surface of all Fe$_3$O$_4$ seeds With the HAuCl$_4$/OLA ratio of 0.25:1, there are many large particles besides the smaller ones (Figure 1e), all of which have Au coatings. This phenomenon showed that in the sample the Ostwald mechanism was predominant, in which the small crystals or thin layer of Au with high energy are recrystallized into the larger crystal forming low energy particles (Ostwald ripening).

The formation of Fe$_3$O$_4$@Au hybrid nanostructure was also confirmed through UV-Vis absorption spectrum at concentration of Au 0.025; 0.0375; 0.05 and 0.0625 mmol Au, respectively (Figure 2c). In the range of wavelength 400–850 nm, Fe$_3$O$_4$ NPs have no absorption peak, and Au NPs show a surface plasmon resonance (SPR) peak at 520 nm, but the samples of Fe$_3$O$_4$@Au
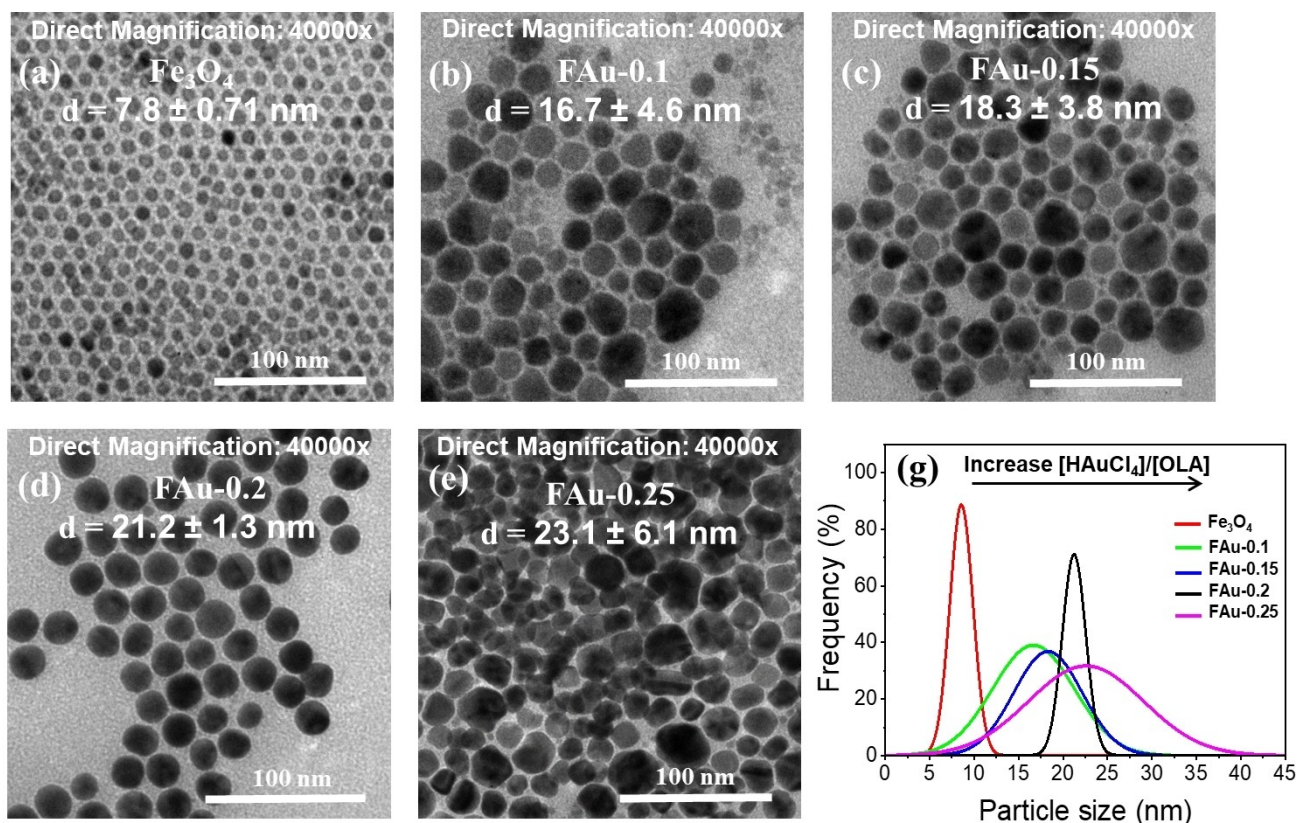
ChemistrySelect

Full Papers
doi.org/10.1002/slct.202102791

Chemistry
Europe
European Chemical
Societies Publishing

Figure 1. The typical TEM images of Fe_3O_4 NPs (a), Fe_3O_4@Au hybrid NPs prepared from different molar ratios $HAuCl_4$/OLA (b–e), and (g) the corresponding size distribution histograms (Scale bar: 100 nm; Direct magnification: 40000x).

hybrid NPs showed an absorption maximum in the wavelength range 529–558 nm, with redshifts of different degrees compared to the SPR peaks of Au NPs. This change is due to the local dielectric effect according to the Mie theory,[25,26] indicating the formation of a hybrid structure between Au and Fe_3O_4. The changes of the surface plasmon resonance properties of the hybrid particles may be explained by the change in the surface electronic properties of the components in the hybrid system. Yang et al. have shown that, if the electrons on the precious metal nanoparticle surfaces are abundant leading to a blue-shift of the SPR position, while the lack of electrons causes a red-shifting.[27] Fe_3O_4 NPs are an electron-deficient component compared to Au NPs, so in the hybrid system, electrons will be transferred from Au to Fe_3O_4, causing electron deficiency on the surface of Au nanoparticles. Therefore, the shift of the SPR in the UV-vis spectra indicates the formation of of the Au shell on the Fe_3O_4 core. This is completely consistent with the observed results from TEM images. In addition, energy-dispersive X-ray spectroscopy (EDS) analysis of the representative sample FAu-0.2 further confirmed the existence of Fe, Au and O elements in the hybrid structure with surface layer are the predominant Au element (Figure 2d). This result demonstrated that Fe_3O_4@Au HNPs with core-shell structure were fabricated successfully. Due to the high uniformity in size, shape and single dispersion, FAu-0.2 sample was used to study other properties of Fe_3O_4@Au hybrid nanostructures.

Figure 2a shows the powder X-ray diffraction patterns of Fe_3O_4, Au and Fe_3O_4@Au nanoparticles. The diffraction maximums at 2-theta are 30.16°, 35.49°, 43.01°, 53.78°, 57.21° and 62.73° (the bottom blue pattern) in according to the families of planes (220), (311), (400), (422), (511), and (440), respectively, indicated the magnetite structure of Fe_3O_4 NPs (JCPDS No. 19–0629). The XRD patterns of the samples Au NPs and Fe_3O_4@Au NPs (sample FAu-0.2) have only a set of peaks at 2-theta of 38.1°, 44.3° 64.5°, and 77.7° corresponding to the crystal plane families (111), (200), (220) and (311), respectively, of the face-centered cubic (fcc) structure of Au NPs (JCPDS No. 04-0784).[28–30] This can be explained by the fact that the Fe_3O_4 coreis completely covered by Au shell (as observed by the TEM image - Figure 2d). This result is also consistent with Chin-Wei Lin's previous report on Fe_3O_4@Au core-shell structure.[31]

The crystallite size of the Au phase was calculated from XRD data using Debye–Scherrer equation:

$$d = \frac{K\lambda}{\beta cos\theta} \quad (1)$$

where, K is a shape factor (0.89 for spherical shape), θ is the Bragg angle, λ is the X-ray wavelength, and β represents the full width at half maximum (FWHM) of the peak. The obtained average crystallite size is approximately 15.1 nm, in consistent with size and structure of the nanoparticles determined from
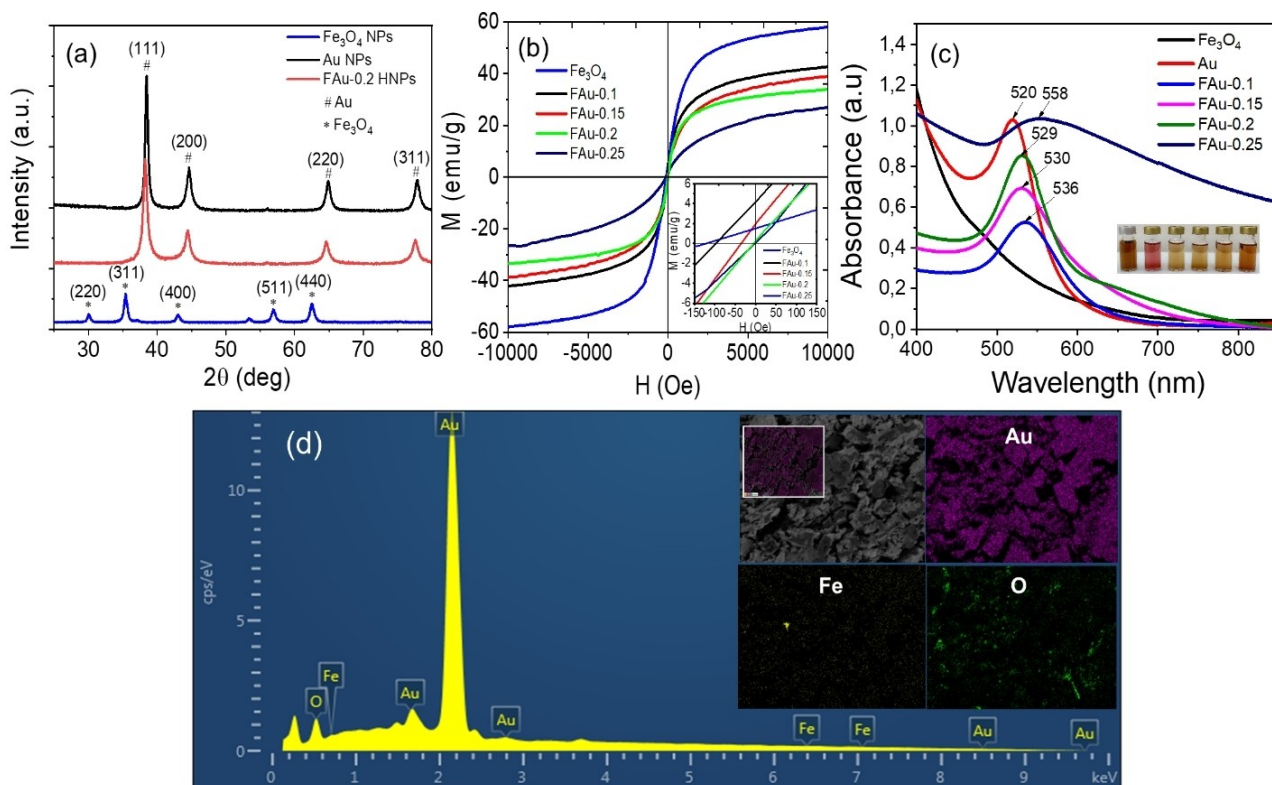
ChemistrySelect

Full Papers
doi.org/10.1002/slct.202102791

Chemistry
Europe
European Chemical
Societies Publishing

Figure 2. (a) XRD patterns of Fe_3O_4 NPs (blue), Au NPs (black) and Fe_3O_4@Au hybrid NPs (red); (b) M(H) curves measured for Fe_3O_4 NPs, Fe_3O_4@Au hybrid NPs samples (inset is the enlarged hysteresis loop at low magnetic field); (c) UV-vis absorption spectra of Fe_3O_4, Au and Fe_3O_4@Au hybrid NPs; and (d) EDS spectra of FAu-0.2 sample.

TEM images, in which multicore-shell structure with cores are Fe_3O_4 seeds (about 7.8 nm), and outer shell is Au metal covered on some cores Fe_3O_4 as confirmed by XRD patterns.

Magnetic property of Fe_3O_4 nanoparticles in the presense of external magnetic fields from −10 kOe to 10 kOe, is presented in Figure 2b. The results showed that the synthesized Fe_3O_4 NPs and Fe_3O_4@Au hybrid nanoparticles are superparamagnetic at the room temperature (Figure 2b). The magnetization saturation decreased from 58.61 emu/g (for Fe_3O_4 sample) to 27.45 emu/g (for FAu-0.25 sample) with increasing the amount of non-magnetic gold shell. Initially, the coercive fields value (H_c) changed little in the FAu-0.1 hybrid sample, compared to that in the Fe_3O_4 sample but then decreased rapidly with further increase of Au concentration. The highest values of coercive fields value (H_c) are 120.5 Oe, 100 Oe for samples Fe_3O_4, FAu-0.1, respectively, and 5.8 Oe, 2.1 Oe for samples reducing FAu-0.2; FAu-0.25, respectively. Generally, the coercive force of nanoparticles depends on the crystal anisotropy, the interactions between the particles, and the particle size and shape.[32]

2.2. Particle size and stability of the PAA-coated Fe_3O_4@Au HNPs

Fe_3O_4@Au HNPs are covered by a hydrophobic layer of OA and OLA in the reaction mixture, so they dispersed well in a less

polar organic solvents, but not in water as requirement for biological purposes. After treatment with hydrophilic PAA, the PAA surface functionalization of FAu-0.2 sample produced highly dispersed particles in water (Scheme 1S). The TEM images of the PAA-encapsulated Fe_3O_4@Au HNPs (here in after denoted as Fe_3O_4@Au@PAA) are shown in Figure 3a. As illustrated, the hybrid nanoparticles were well dispersed without any agglomeration. The hydrodynamic diameter 52 nm and zeta potential value of −34.9 mV (Figure 3c) was determined by DLS method in simulated physiological conditions in the human body (pH 7.4, [NaCl] = 156 mM) at a high concentration of 3 mg/mL, showing that the hybrid Fe_3O_4@Au@PAA HNPs have good properties in size and stability for biological applications.

2.3. In vitro cytotoxicity results

Due to the potential applications in biological systems, cytotoxicity test is an important step to access the biocompatibility of Fe_3O_4@Au@PAA. Therefore, a range of concentrations of Fe_3O_4@Au@PAA from 5 µg/mL to 100 µg/mL was tested by applying SRB assay on Hep-G2, human liver cancer cell line and Vero, monkey kidney normal cell line. As two control conditions, DMSO and Ellipticine showed expected results with 100% cell survived in the former and no cancer cell survived in samples treated with the later (Figure 4a). Noticeably,
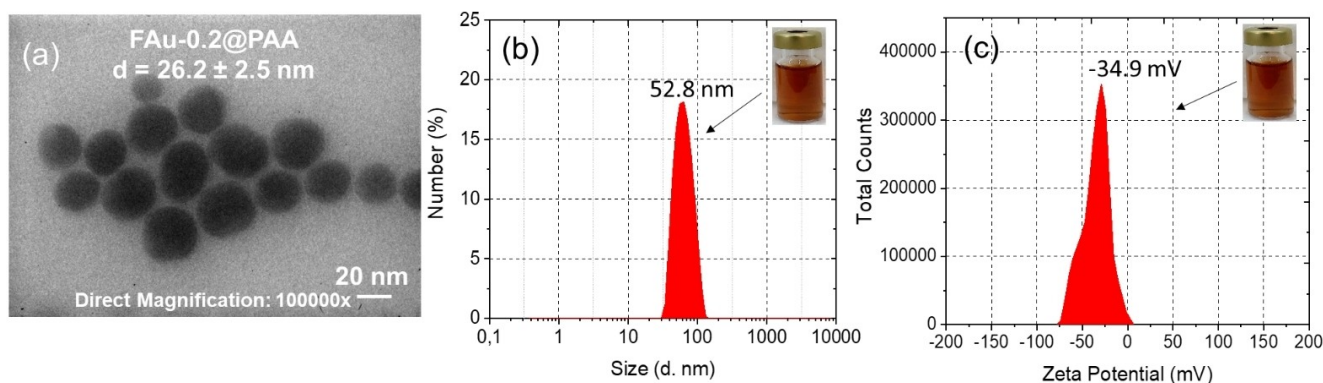
ChemistrySelect

Full Papers
doi.org/10.1002/slct.202102791

Chemistry
Europe
European Chemical
Societies Publishing

Figure 3. The typical TEM images (Scale bar: 20 nm; Direct Magnification: 100000x) (a); Size distribution (b); and Zeta potentials of the PAA-coated Fe_3O_4@Au hybrid NPs (c).
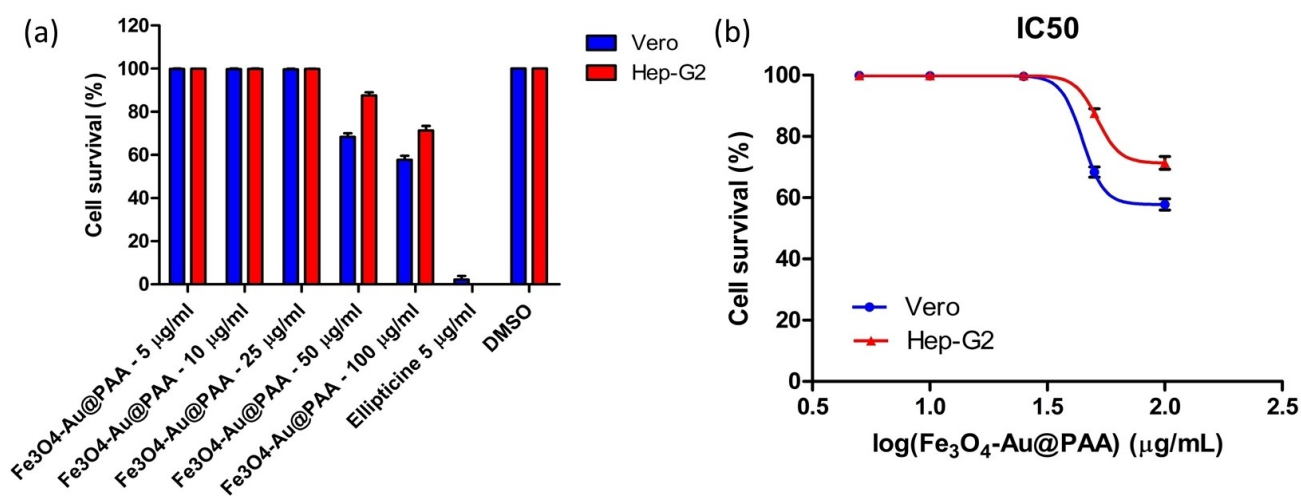

Figure 4. Cytotoxicity of Fe_3O_4@Au@PAA on HepG2 and Vero. (a) Percentage of cell survive of samples incubated with Fe_3O_4@Au@PAA (5–10–25–50–100 μg/ mL); DMSO 10% and Ellipticine (5 μg/mL); and (b) IC_{50} curve with log concentration of Fe_3O_4@Au@PAA. Graphs were obtained by using GraphPad and data was presented as mean ± SD.

Fe_3O_4@Au@PAA did not cause any impact on cell survival rate or morphology on both two cell lines with 5, 10 and 25 μg/mL (Figure 4, Figure 5). Light influence was shown at higher concentration (50 and 100 μg/mL) but did not exceed 50% of
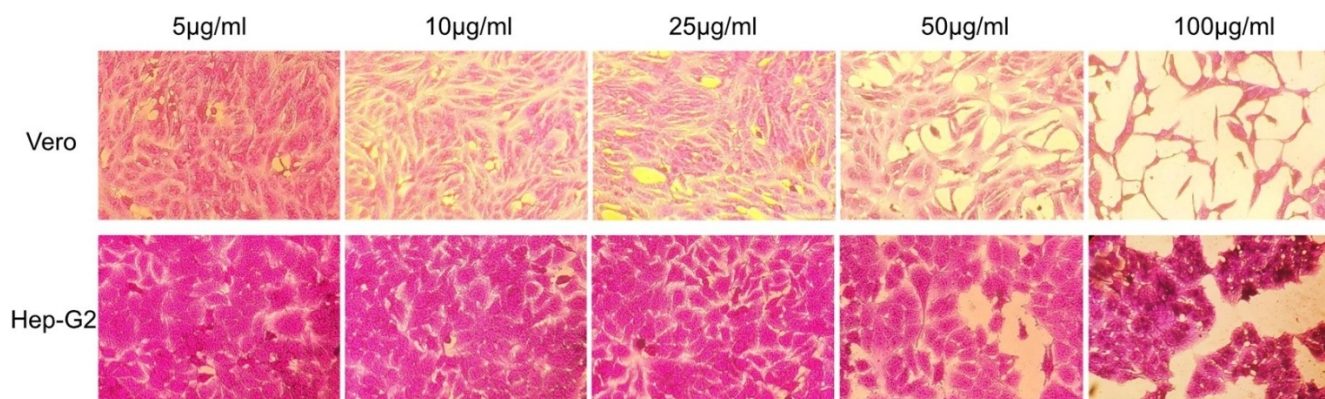

Figure 5. Vero and Hep-G2 cell treated with a range of concentration of Fe_3O_4@Au@PAA. Microscope images were taken with objective lens: 10X.

ChemistrySelect

Full Papers
doi.org/10.1002/slct.202102791

Chemistry Europe
European Chemical
Societies Publishing

cell death, which leaded to the IC_{50} of Fe_3O_4@Au@PAA on Vero and Hep-G2 were 124.7 and 184.9 µg/ml, respectively (Figure 4b).

Gold, with its high biocompatibility, is a promising material to strengthen the application of Fe_3O_4 nanoparticles in biomedicine. Modifications on the Au nanostructure of either size, shape or surface condition and chemical properties would affect the toxicity of this material on cells, organ and body.[33] Cell viabilities on two cell lines Hep-G2 and Vero showed that Fe_3O_4@Au@PAA neither have specific target to human liver cancer cell line Hep-G2 nor cause toxicity to both cell lines. These results suggested that these synthesized gold-magnetic nanoparticles is safe enough for using in CT and MRI techniques as a contrast agent, and other biomedical applications (drug delivery, hyperthermal and photothermal treatment,…). Further in vitro, the in vivo experiments on cell up taken, organ accumulation and elimination should be performed to investigate more deeply the effect of Fe_3O_4@Au@PAA on cells and body.

2.4. Contrast enhancement in vitro MR/CT Imaging

To explore the potential of Fe_3O_4@Au@PAA nanomaterials for use in dual-mode MR/CT imaging, T_2 transverse relaxation time and X-ray attenuation properties of the hybrid NPs were investigated. The role of Fe_3O_4 NPs as an MRI contrast agent is to decrease T_2 transverse relaxation time, thereby increasing transverse relaxation rate r_2. In this study, with small, uniform in size and shape Fe_3O_4 core particles, covered by Au shell, the T2-weighted MRI transverse relaxation rate r_2 measurements of Fe_3O_4@Au@PAA hybrid nanoparticles were performed to evaluate its applicability as a contrast agent for MRI imaging (Figure 6a–b). Figure 6a-b showed that increasing in Fe concentration led to increase in the intensity of the MRI signal (negative contrast). To evaluate T2-weighted contrast feature (T2 W), the experiments were performed at different values of the TE pulse. Figure 6b showed the T2-weighted MRI image signal intensity at different concentrations of Fe_3O_4@Au@PAA nanoparticles and different values of echo time TE. It is easy to notice a significant contrast even when the difference in the concentration is relatively small.
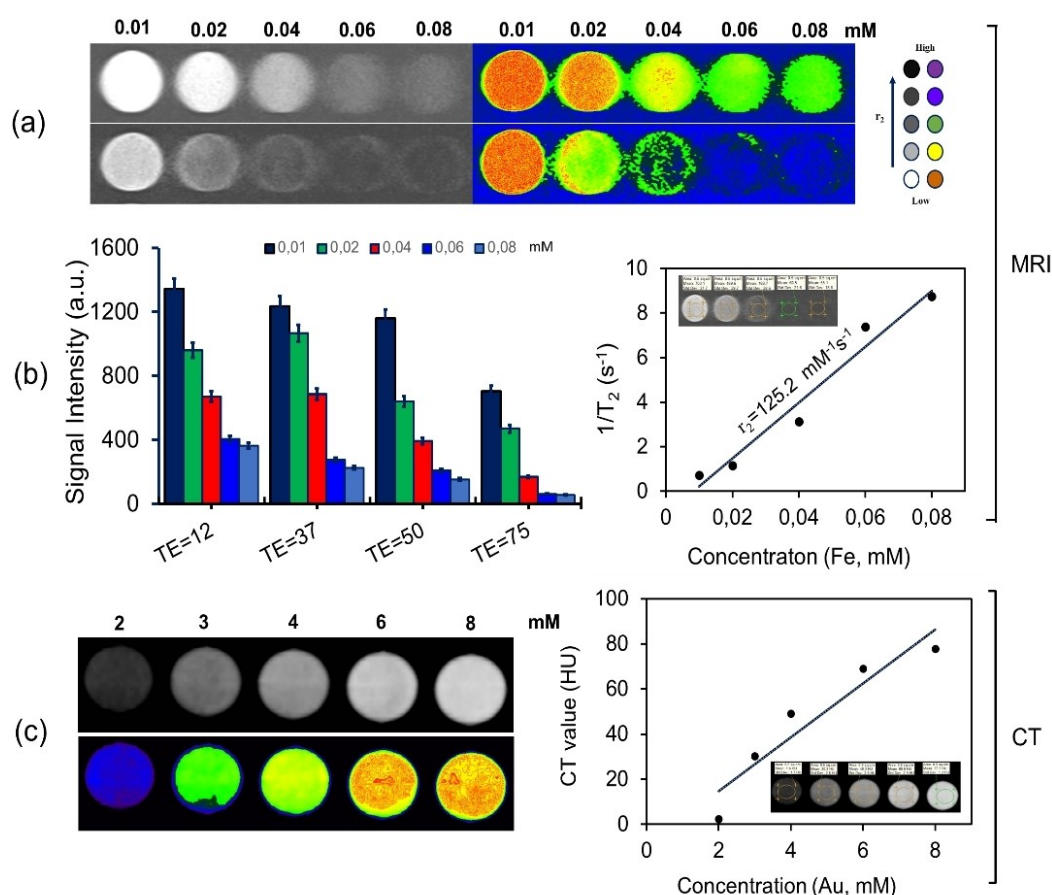

Figure 6. T_2 - weighted MRI and r_2 color maps in the presence of Fe_3O_4@Au@PAA at different conditions, (a) TE = 12 ms, TE = 75 ms, TR = 3000 ms; (b) MRI signal intensity at the different concentrations in 1.5% agarose solution of the HNPs at the different values of TE, (The error bars represent the standard deviation) (left), and $1/T_2$ (R_2) - Fe concentration plot of the Fe_3O_4@Au@PAA HNPs at 1.5T (right); and (c) In vitro CT images of the Fe_3O_4@Au@PAA HNPs at different Au concentrations (left), and the X-ray attenuation intensity of the Fe_3O_4@Au@PAA HNPs as a function of the Au concentration (right) (Inset: CT image of the different concentrations of Fe_3O_4@Au@PAA HNPs).

ChemistrySelect

Full Papers
doi.org/10.1002/slct.202102791

Chemistry Europe
European Chemical
Societies Publishing

The transverse relaxation rate r_2 was determined by the linear equation of $1/T_2$ to the iron concentrations (in mM) (Figure 6b), with the slope is correlatively the transverse relaxation rate (r_2) 125.2 $mM^{-1}s^{-1}$. The r_2 value is lower than that of our previously published Fe_3O_4 NPs researches,[22,34] which can be explained by the thick nonmagnetic Au layer coating on the magnetic Fe_3O_4 core, but is much higher than that of Fe_3O_4@Au HNPs reported in previously articles,[20,35–37] especially our fabricated materials that has a higher uniformity in size, shape and dispersion than many published reports (Table 1).[13,38–40] These findings suggested that our synthesized Fe_3O_4@Au@PAA hybrid nanoparticle can be used as a T_2 transverse relaxation time shortening agent for the MRI applications.

The use of Au NPs as CT contrast agents is notable because they are better X-ray attenuation than iodine-based ones.[41] Similar to the MRI image signal acquisition technique, in the CT imaging technique the HU values of the obtained images will be analyzed directly using eFilm workstations software (Merge Healthcare, Chicago, IL, USA) based on the intensity of the signal of the received ROI (shown by the colored circle in Figure 6c). Figure 6c showed the CT image when using Fe_3O_4@Au@PAA hybrid NPs at different Au concentrations (left) and the line diagram of the Hounsfield unit relative to the Au concentration (right). The results showed that, as Au concentration increased, the CT image intensity increased linearly, corresponding to the increased Hounsfield intensity value. In the color map of CT images encoded with Hounsfield (HU) value, X-ray attenuation levels are shown relative in purple and yellow-orange (Figure 6c).

In comparison with MR imaging technique, CT expresses low sensitivity in the absence of contrast agent, and is therefore limited in use. The X-ray attenuation of Fe_3O_4@Au@PAA HNPs increased linearly with Au concentration. Figure 6c describes a clearly contrast for the samples with Au concentrations from 3 mM to 6 mM, in which the X-ray absorption capacity increased linearly, corresponding to a strong increase in signal intensity from 30.3 HU to 68.6 HU (2.26 times). The quantification based on average grayscale value table showed a good linear relationship between the obtained CT contrast ratio and nanoparticle concentrations (Figure 6c). The metal composition of Fe_3O_4@Au@PAA HNPs (FAu0.2 sample) was determined quantitatively by ICP-MS method, showed that mole ratio of the Fe/Au is 3.2:1, and is much higher than that of Fe_3O_4@Au HNPs in the previous reports.[39] Compared to the X-ray attenuation characteristics of the Omnipaque and nano Au contrast agents reported in the other studies,[42–44] the X-ray attenuation property of the our Fe_3O_4@Au@PAA HNPs in our research is higher. As a comparison, in the research of Linfeng Zheng et al.,[45] the signal intensity at the Au and I concentration of 20 mM is about 140 HU and 80 HU, respectively. In our research, at a Au concentration of 8 mM, the obtained signal intensity was 77.7 HU. In another research of Tingting Xiao et al., the results showed that the signal intensity (X-ray attenuation ability) of Au NPs and Omnipaque nanomaterials according to the iodine concentration corresponds to much higher concentration than our research.[46] This research determines that the X-ray attenuation property of our Fe_3O_4@Au@PAA HNPs higher than that of the Omnipaque contrast agent.[21] In CT technique, materials with high density ρ or large atomic number Z able to strongly absorb X-rays, as the following formula represents the coefficient for X-ray absorption μ depended on Z:[47]

$$\mu \approx \frac{\rho Z^4}{AE^3} \tag{2}$$

Table 1. Transverse relaxation rate r_2 of Fe_3O_4@Au@PAA and commercial Fe_3O_4 nanoparticle-based MRI contrast agents.						
Brand name	Ligand shell	Core size/Hydrodynamic diameter (nm)	r_2 relaxation rate ($mM^{-1}s^{-1}$)	Target	Company/application/ development-phase	Ref.
Ferumoxides (Feridex IV, Endorem), AMI-25	Dextran	5–6 80–150	158	Liver, spleen bone marrow	AMAG Pharmaceuticals Guerbet Approved	[48]
Ferucarbotran (SHU-555 A), Resovist	Carboxydextran	4.2 50–100	189	Liver, spleen bone marrow	Bayer Healthcare Pharmaceuticals/approved EU, Japan, USA	[48]
Au-Fe_3O_4	PEG	20 –	114	–	–	[49]
Fe_3O_4/Aun.Ac-FA NCPs	(PGA)/poly(L-lysine)/ PGA/folic acid (FA)	– 532.5	92.67	Liver, spleen	–	[50]
Fe_3O_4@Au NCPs	poly(g-glutamic acid) (PGA) and poly(L-lysine) (PLL)	– 200	71.55	Liver	–	[39]
Fe_3O_4@Au core-shell	SiO_2	–	61.9	–	–	[20]
Fe_3O_4@SiO_2@Aushell	SiO_2	33 –	87	–	–	[20]
Yolk-shell Fe_3O_4@Au	Au	65 –	149.4	–	–	[20]
Fe_3O_4@Au@PAA	Poly (acrylic acid)	21 52	125.2	Current study	Current study	

ChemistrySelect

Full Papers
doi.org/10.1002/slct.202102791

Chemistry Europe
European Chemical
Societies Publishing

where: A, E are atomic weight, and energy of X-ray, respectively.

By the larger of Z and ρ than that of iodine, gold has a theoretical X-ray attenuation 2.7 times higher than that of iodine (gold, 5.16 cm²/g; iodine, 1.94 cm²/g).[41] In comparison with single Au NPs, the X-ray attenuation ability of Fe_3O_4@Au@PAA is higher, suggesting that the core-shell structure helps to achieve a larger surface area since the amount of Au only covers the outer layer on surface of the core Fe_3O_4.

The high transverse relaxation rate r_2 and good X-ray attenuation properties of the fabricated Fe_3O_4@Au HNPs, along with their good cytoplasmic compatibility, prompted us to further explore their use as a dual-mode MRI/CT imaging contrast agent for *in-vivo* tests.

In the *in-vivo* experiments, after injection of 0.1 mL Fe_3O_4@Au HNPs ([Fe] = 8.33 mg mL⁻¹, [Au] = 2.85 mg mL⁻¹) into the mouse-tail vein, MR scanning process was performed. Figure 7a showed T2-weighted *in-vivo* MR images of mouse

liver before and after injection Fe_3O_4@Au@PAA HNPs at 10, 30, 60 and 120 min, respectively. It is clear that the liver ROI (indicated by the red circle) darkens significantly and becomes darkest 30 min after injection. The liver MR images then started to become brighter after 90 min of scanning, this may because of Fe_3O_4@Au HNPs undergoing a further metabolism and has differences in biodistribution over time, corresponding to Fe concentration in liver tissue gradually decreased. Quantitative signal intensity of liver tissue has a changes as a function of time after injection of Fe_3O_4@Au@PAA HNPs fluid as contrast agents. Specifically, at 10 min after injection, the mouse liver showed a decrease in the intensity of the MR T_2 signal (122.9 pixel) when compared with the original signal before injection (145.6 pixel). The signal changed more strongly at time points 30 (34.7 pixel) after injection. Thereafter, the signal intensity gradually recovered to 61.5 and 126.7 pixel, respectively at 60 and 120 min after injection. The signal changes in the liver can be understood because when nanoparticles are injected in the veins, portions of the nanoparticles are isolated by the liver
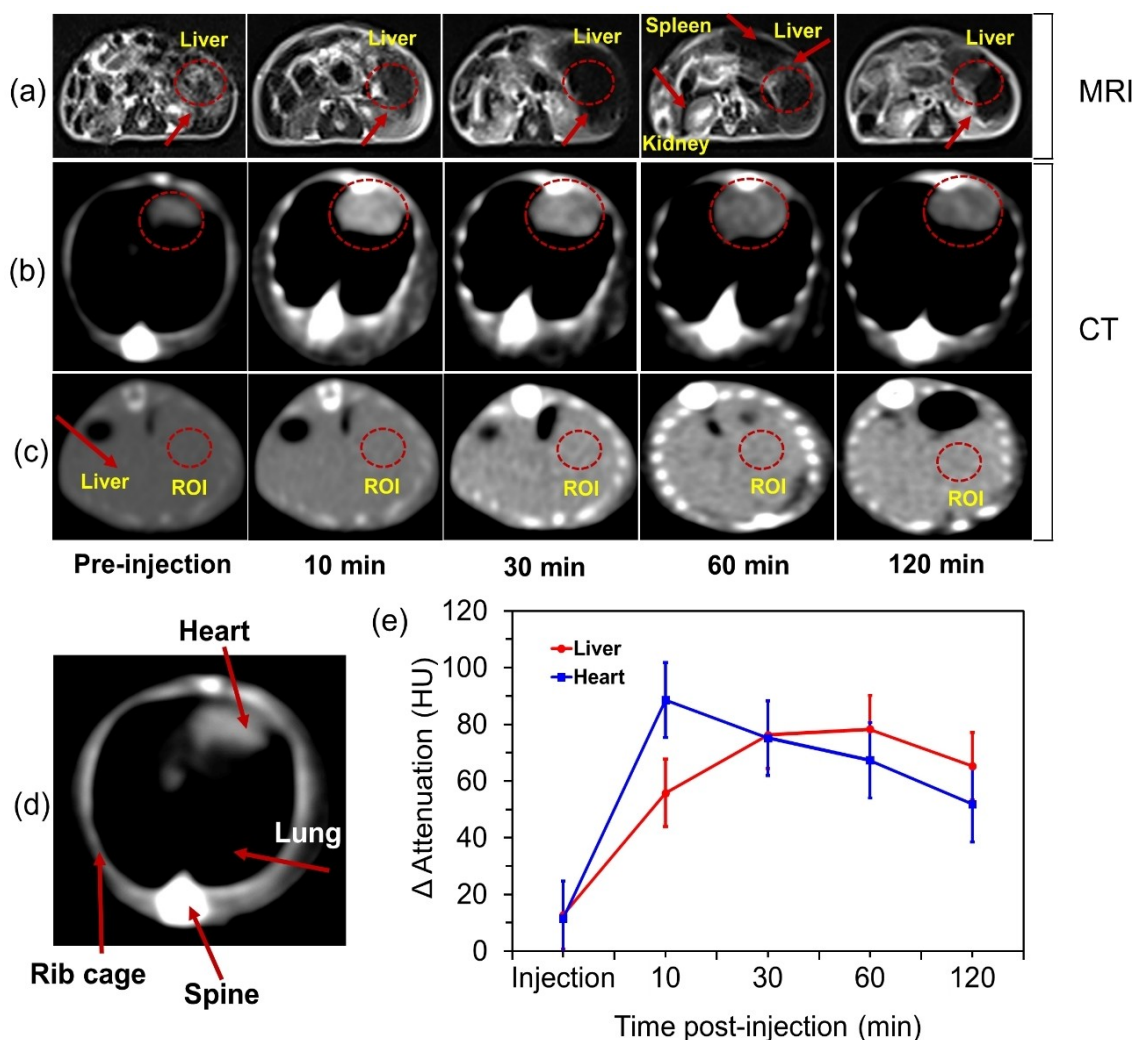

Figure 7. *In vivo* T_2-weighted MR images of the liver, kidney and spleen of a mouse (a); Time evolutional in vivo CT imaging of mouse heart and liver using magneto-plasmonic hybrid nanofluid Fe_3O_4@Au@PAA (b–d); and (e) CT attenuation change of different organs over time: pre- and 10, 30, 60, and 120 minutes post-injection (red circle) sites. The error bars represent the standard deviation.

ChemistrySelect

Full Papers
doi.org/10.1002/slct.202102791

Chemistry Europe
European Chemical
Societies Publishing

through the reticuloendothelial system. Surface modification by the -COOH groups of HNPs allowed them to escape absorption by the last reticuloendothelial system (RES), corresponding to the recovery signal intensity, which would facilitate them to accumulate in other tissues through a passive targeting way based on enhanced permeability and retention effects (EPR).[51] Our results showed that the fabricated Fe_3O_4@Au HNPs can be used as a T_2-negative contrast agent for imaging mouses liver MRI.

Nextly, to explore the CT imaging capabilities of Fe_3O_4@Au@PAA HNPs, 0.3 mL of the fluid was injected into the mouse tail vein (corresponding to a concentration [Fe] = 8.33 mg mL^{-1}, [Au] = 2.85 mg mL^{-1}). CT images were collected at different periods after injection (Figure 7b–e). Contrast effects are inspected major organs (heart and liver). Figure 7b–c is a CT image of the mouse heart before injection. There was a significant difference in signal intensity at the heart after 10 min of injection, with increasing from 11.5 HU to 88.5 HU, then decreasing over time, in proportion to the amount of blood leaded contrast agents to other tissues in the body (Figure 7b). Meanwhile, similar to the MR images, the signal CT of liver tissue also changes strongly after 10 minutes and is strongly enhanced at 30 minutes after injection, corresponding to values of 55.8 and 76.3 HU respectively, compared to 12.7 HU before injection (Figure 7c, e). Generally, our results found that the Fe_3O_4@Au@PAA HNPs can be used as a contrast agent for dual-mode MR/CT imaging applications. It should be noted that the mouses alived normally and had no undesirable side effects after injection, showing that Fe_3O_4@Au@PAA HNPs injection did not exhibit any significant *in-vivo* cytotoxicity.

3. Conclusions

In summary, Fe_3O_4@Au core-shell structure magneto-optical hybrid nanomaterials have been successfully synthesized by thermal decomposition combined with seed mediated growth method, using high quality Fe_3O_4 nanoparticles (small size, monodisperse) as a plasm for the synthesis of Fe_3O_4@Au hybrid nanoparticles. The effect of the ratio of $HAuCl_4$ and oleyamin (OLA) precursors on the shape, size and uniformity of the materials was studied to find the optimal conditions. The results showed that the Fe_3O_4@Au core-shell hybrid nanoparticles have a spherical shape with a thick Au shell at the outside, an average particle size of 21 nm, monodisperse and good magnetic response. Magneto-plasmonic hybrid nanoparticles after denatured surface with polyacrylic acid (PAA) have high stability in aqueous solution with zeta potential −34.9 mV, hydrodynamic size (DLS) 52.8 nm. Fe_3O_4@Au@PAA magneto-plasmonic hybrid nanofluid is non-toxic to the Hep-G2 cancer cell line Vero healthy cell line, with high stability in physiological conditions. The *in-vitro* test results of dual-mode MR/CT images showed that the value of transverse relaxation rate r_2 is 125.2 mM^{-1}s^{-1} and good X-ray attenuation ability even at low concentrations. The *in-vivo* test on mouse showed that the images of body parts were clearly observed after injection of Fe_3O_4@Au@PAA with T2-weighted imaging, as well as CT images. Especially, the body's hiding ability from the

reticuloendothelial system (RES) has increased the circulation time of the contrast agent in the body. With these outstanding properties, the high quality Fe_3O_4@Au@PAA magneto-plasmonic hybrid nanofluid prepared in this research showed great promise as a candidate for multimodal bioimaging techniques in real application.

Supporting Information Summary

The Supporting Information includes the detailed experimental section of this work

Conflict of Interest

The authors declare no conflict of interest.

[1] J. Garcia, T. Tang, A. Y. Louie, *Nanomedicine.* **2015**, *10*, 1343–1359.
[2] J. Bussink, J. H. A. M. Kaanders, W. T. A. Van Der Graaf, W. J. G. Oyen, *Nat. Rev. Clin. Oncol.* **2011**, *8*, 233–242.
[3] S. He, N. J. J. Johnson, V. N. H. Anh, E. Cory, Y. Huang, R. Sah, J. V. Jokerst, A. Almutair, *Nano Lett.* **2017**, *17*, 4873–4880.
[4] A. Polyak, T. L. Ross, *Curr. Med. Chem.* **2018**, *25*, 4328–4353.
[5] S. Parka, H. Kima, S. C. Lima, K. Lima, E. S. Leeb, K. T. Ohc, H. G. Choid, Y. S. Youn, *J. Controlled Release* **2019**, *304*, 7–18.
[6] M. A. Dheyab, A. A. Aziz, M. S. Jameel, O. A. Noqta, P. M. Khaniabadi, B. Mehrdel, *Mater. Today Commun.* **2020**, *25*, 101368.
[7] W. Feng, X. J. Zhou, W. Nie, L. Chen, K. X. Qiu, Y. Z. Zhang, C. L. He, *ACS Appl. Mater. Interfaces* **2015**, *7*, 4354–4367.
[8] S. M. Park, A. Aalipour, O. Vermesh, J. H. Yu, S. S. Gambhir, *Nat. Rev. Mater.* **2017**, *2*, 17014.
[9] T. H. Shin, Y. Choi, S. Kim, J. Cheon, *Chem. Soc. Rev.* **2015**, *44*, 4501–4516.
[10] N. Singh, G. J. S. Jenkins, R. Asadi, S. H. Doak, *Nano Rev.* **2010**, *1*, 5358.
[11] A. S. Thakor, J. V. Jokerst, P. Ghanouni, J. L. Campbell, E. Mittra, S. S. Gambhir, *J. Nucl. Med.* **2016**, *57*, 1833–1837.
[12] J. W. M. Bulte, *Am. J. Roentgenol.* **2009**, *193*, 314–325.
[13] M. Keshtkar, D. S. Gahrouei, A. Mahmoudabadi, *J. Med. Signals Sens.* **2020**, *10*, 201–207.
[14] G. Wang, W. Gao, X. Zhang, X. Mei, *Sci. Rep.* **2016**, *6*, 1–10.
[15] N. T. Dung, N. T. N. Linh, D. L. Chi, N. T. H. Hoa, N. P. Hung, N. T. Ha, P. H. Nam, N. X. Phuc, L. T. Tam, L. T. Lu, *RSC Adv.* **2021**, *11*, 13458–13465.
[16] E. Fantechi, A. G. Roca, B. Sepúlveda, P. Torruella, S. Estradé, F. Peiró, E. Coy, S. Jurga, N. G. Bastús, V. Puntes, V. Puntes, *Chem. Mater.* **2017**, *29*, 4022–4035.
[17] C. Xu, X. Jin, H. Don, C. Wang, N. Kohler, E. G. Walsh, J. R. Morgan, Y. E. Chin, S. Sun, *Angew. Chem. Int. Ed..* **2008**, *47*, 173–176.
[18] E. Fantechi, A. G. Roca, B. Sepúlveda, P. Torruella, S. Estradé, F. Peiró, E. Coy, S. Jurga, N. G. Bastús, V. Puntes, V. Puntes, *Chem. Mater.* **2017**, *29*, 4022–4035.
[19] Y. Jin, C. Jia, S. W. Huang, M. O'Donnell, X. Gao, *Nat. Commun.* **2010**, *1*, 1–8.
[20] L. S. Lin, X. Yang, Z. Zhou, Z. Yang, O. Jacobson, Y. Liu, A. Yang, G. Niu, J. Song, H. H. Yang, X. Chen, *Adv. Mater.* **2017**, *29*, 1606681.
[21] J. Li, L. Zheng, H. Cai, W. Sun, M. Shen, G. Zhang, X. Shi, *ACS Appl. Mater. Interfaces.* **2013**, *5*, (20), 10357–10366.

[22] L. T. Tam, H. N. Du, T. N. N. Linh, P. T. H. Tuyet, H. D. Quang, N. T. Vuong, L. T. T. Hiep, V. T. K. Oanh, L. H. Khoa, L. D. Duong, L. T. Lu, T. D. Lam, *ChemistrySelect*. **2020**, *5*, 12915–12923.

[23] V. T. K. Oanh, L. T. Tam, D. H. Doan, N. X. Truong, N. X. Ca, V. T. Thu, L. T. Lu, T. D. Lam, *Mater. Chem. Phys.* **2020**, *245*, 122762.

[24] V. T. K. Oanh, T. D. Lam, V. T. Thu, L. T. Lu, P. H. Nam, L. T. Tam, D. H. Manh, N. X. Phuc, *J. Electron. Mater.* **2016**, *45*, 4010–4017.

[25] Y. Tang, X. Yu, J. Xu, B. Audit, S. Zhang, *Elsevier Inc.* **2019**, *20*, 431–455.

[26] P. Singh, C. Upadhyay, *Mater. Res. Express.* **2017**, *4*, 105401.

[27] D. Yang, X. Pang, Y. He, Y. Wang, G. Chen, W. Wang, Z. Lin, *Angew. Chem. Int. Ed.* **2015**, *54*, 12091–12096; *Angew. Chem.* **2015**, *127*, 12259–12264.

[28] G. Geng, P. Chen, B. Guan, Y. Liu, C. Yang, N. Wang, M. Liu, *RSC Adv.* **2017**, *7*, 51838–51846.

[29] T. H. Lin, C. W. Lin, H. H. Liu, J. T. Sheu, W. H. Hung, *Chem. Commun.* **2011**, *47*, 2044–2046.

[30] M. Abbas, S. R. Torati, C. G. Kim, *Dalton Trans.* **2017**, *46*, 2303–2309.

[31] L. C. Wei, J. M. Chen, Y. J. Lin, L. W. Chao, S. Y. Wei, C. H. Wu, C. C. Jeng, L. M. Wang, K. L. Chen, *Sci. Rep.* **2019**, *9*, 16466.

[32] P. Puliová, J. Kováč, A. Voigt, P. Raschman, *J. Magn. Magn. Mater.* **2013**, *341*, 93–99.

[33] P. Skehan, R. Storeng, D. Scudiero, A. Monks, J. Mcmahon, D. Vistica, J. T. Warren, H. Bokesch, S. Kenney, M. R. Boyd , *J. Natl. Cancer Inst.* **1990**, *82*, 1107–1112.

[34] L. T. Tam, N. H. Du, N. T. N. Linh, N. T. Vuong, P. T. H. Tuyet, N. T. H. Hoa, N. Q. Thang, H. T. Ha, D. T. Chien, B. L. Minh, L. T. Lu, L. D. Duong, S. V. Bhosale, T. D. Lam, *J. Nanosci. Nanotechnol.* **2020**, *20*, 5338–5348.

[35] C. Caro, F. Gámez, P. Quaresma, J. M. P. Muñoz, A. Domínguez, J. R. Pearson, M. P. Leal, A. M. Beltrán, Y. F. Afonso, J. M. D. Fuente, R. Franco, E. Pereira, M. L G. Martín, *Pharmaceutica* **2021**, *13*, 1–21.

[36] T. Zhou, B. Wu, D. Xing, *J. Mater. Chem.* **2012**, *22*, 470–477.

[37] E. Umut, F. Pineider, P. Arosio, C. Sangregorio, M. Corti, F. Tabak, A. Lascialfari, P. Ghigna, *J. Magn. Magn. Mater.* **2012**, *324*, 2373–2379.

[38] E. D. Smolensky, M. C. Neary, Y. Zhou, T. S. Berquo, V. C. Pierre, *Chem. Commun.* **2011**, *47*, 2149–2151.

[39] H. Cai, K. Li, M. Shen, S. Wen, Y. Luo, C. Peng, G. Zhang, X. Shi, *J. Mater. Chem.* **2012**, *22*, 15110–15120.

[40] A. R. Montazerabadi, M. A. Oghabian, R. Irajirad, S. Muhammadnejad, D. Ahmadvand, H. H. Delavari, S. R. Mahdavi, *NANO* **2015**, *10*, 1550048.

[41] J. F. Hainfeld, D. N. Slatkin, T. M. Focella, H. M. Smilowitz, *Br. J. Radiol.* **2006**, *79*, 248–253.

[42] C. Peng, L. Zheng, Q. Chen, M. Shen, R. Guo, H. Wang, X. Cao, G. Zhang, X. Shi, *Biomaterials.* **2012**, *33*, 1107–1119.

[43] Q. Chen, K. Li, S. Wen, H. Liu, C. Peng, H. Cai, M. Shen, G. Zhang, X. Shi, *Biomaterials.* **2013**, *34*, 5200–5209.

[44] H. Liu, Y. Xu, S. Wen, Q. Chen, L. Zheng, M. Shen, J. Zhao, G. Zhang, X. Shi, *Chem. A Eur. J.* **2013**, *19*, 6409–6416.

[45] L. Zheng, J. Zhu, M. Shen, X. Chen, J. R. Baker, S. H. Wang, G. Zhang, X. Shi, *MedChemComm* **2013**, *4*, 1001–1005.

[46] T. Xiao, S. Wen, H. Wang, H. Liu, M. Shen, J. Zhao, G. Zhang, X. Shi, *J. Mater. Chem. B.* **2013**, *1*, 2773–2780.

[47] P. S. Miedema, *Raman Spectrosc. Appl.* **2017**, *11*, 225–246.

[48] H. Ittrich, K. Peldschus, N. Raabe, M. Kaul, G. Adam, *Fortschr Röntgenstr.* **2013**, *185*, 1149–1166.

[49] H. B. Na, I. C. Song, T. Hyeon, *Adv. Mater.* **2009**, *21*, 2133–2148.

[50] H. Cai, K. Li, J. Li, S. Wen, Q. Chen, M. Shen, L. Zheng, G. Zhang, X. Shi, *Small* **2015**, *11*, 4584–4593.

[51] H. Liu, H. Wang, Y. Xu, M. Shen, J. Zhao, G. Zhang, X. Shi, *Nanoscale.* **2014**, *6*, 4521–4526.